Phase field crystal modeling of grain boundary structures in diamond cubic systems

Kevin H. Blixt ● * and Håkan Hallberg ●
Division of Solid Mechanics, Lund University, P.O. Box 118, SE-221 00 Lund, Sweden

Phase field crystal (PFC) modeling has proved to be a versatile numerical tool in the analysis of crystalline microstructures. Most often, however, the focus is put on bulk crystal behavior, while crystal defects such as grain boundaries (GBs) are less explored. This is, in particular, the case for crystal structures beyond fcc and bcc. In this work, the possibilities and challenges in adopting PFC to diamond cubic (DC) crystal structures is investigated. Three different PFC models are considered for this purpose. One of them was published previously, and two are modifications proposed in the present work. The models are compared in terms of both DC phase stabilization and their ability to provide relevant GB structures. The models employ combinations of two- and three-point correlations, and the addition of a three-point correlation is found to be required for stabilization of the expected DC GB structures. It is concluded that although each of the models has limitations in terms of the GB structures which can be stabilized and performance in terms of phase stability, key PFC components for successful modeling of DC structures can be identified.

I. INTRODUCTION

Extending the phase field crystal (PFC) method to more involved crystal structures, beyond fcc and bcc, continues to be a main driver for PFC development. Being able to model the diamond cubic (DC) crystal structure is particularly desirable due to its prevalence in materials of technological significance, such as silicon, which is critical in applications like integrated circuits and solar cells. In these applications, the effect of defect structures and their evolution within the material are of particular interest [1,2]. Aiming at such defect structures, the extended temporal timescales offered by the PFC framework compared to alternative methods such as molecular dynamics (MD) while still retaining atom-scale spatial resolution is particularly attractive. However, the development and use of PFC models for DC structure simulations are, to date, limited and primarily focused on the stabilization of bulk phases, with insufficient consideration of the produced defect structures, such as grain boundaries (GBs), which are pivotal for a wide range of technical applications.

The possibility of studying DC crystals within the PFC framework is not apparent at first glance, as these crystals form through covalent bonding, compared to the metallic bonding of metallic systems usually investigated using PFCs. In DC systems, such as silicon, each atom strives to form bonds with four other atoms in a tetrahedron, forming bond angles of 109.5°. Thus, atoms in a DC crystal tend to form structures that minimize bond angle variation and the presence of dangling bonds, rather than just minimizing excess volume, as is commonly the case for metallic systems [3]. These two aspects are not usually considered in PFC modeling. Models that do consider angular dependences in the atom correlation have been developed, and some relevant models are investigated in the present study. Currently, four main PFC models for achieving a DC structure are known to the authors. To begin with, in [4] the DC-relevant peaks for the two-point correlation used in the structural phase field crystal (XPFC) method were identified. This model was later used in [5] to study dislocation half loops. However, the model includes only a two-point correlation without an explicit angle dependency.

The lack of angle dependence was later addressed by another model, developed in [6], where a three-point correlation was introduced to target certain angles between reciprocal vectors. The discussion in [6] on the properties of the DC model is brief, however, and the authors expressed that there was some difficulty in stabilizing the DC lattice structure.

More recently, the effects of using up to a four-point correlation on the stabilization and material properties of a wide variety of crystal structures, including a DC structure, were investigated in [7,8]. With up to a four-point correlation, an explicit angle dependence can be formulated between a family of reciprocal vectors while still satisfying the resonant conditions. Of course, by adding higher-order correlations the computational effort is increased compared to using only a two-point correlation.

The last model for DC structure, proposed in [9], is implemented using the amplitude expansion of the phase-field crystal model, a method sometimes referred to as APFC. In APFC, the reciprocal space is reduced to the main crystal symmetries using a multimode approximation. This

---

*Corresponding author: Kevin.Blixt@solid.lth.se

approximation makes even larger domains accessible, but some structural information is lost.

A final notable contribution, although it does not directly target DC structure, is the work presented in [10], where a two-dimensional (2D) three-point correlation function defined in spatial coordinates was introduced. Most important to this work, they successfully replicated graphene polycrystals, achieving GB structures that closely matched those observed in real graphene systems. This result is significant as graphene, like DC, forms through covalent bonding.

In order to limit the scope of this work, only the models presented in [4,6,10] are considered. However, they can be regarded as special cases of the more general model presented in [7,8], restricted up to the three-point correlation. Furthermore, [9] is a limitation of the reciprocal space compared to the other models and is considered to be outside the scope of the present study.

The problem of constructing interaction potentials is not limited to PFCs and appears in many situations, generally termed self-assembly problems, with MD being a notable example. These self-assembly methods have been used to construct potentials that stabilize DC crystals, using both isotropic [11] and nonisotropic [12,13] pair interactions. DC GB structures obtained with MD are considered in the present work for comparison against the PFC results. The Tersoff potential, frequently used in MD studies on DC, is also employed in postprocessing bond networks from the PFC simulations.

As previously noted, DC structures have been studied within the PFC framework, although the focus has primarily been on the stabilization of a homogeneous DC phase and its bulk behavior, without considering the local defect structure ([9] being the exception) such as GBs. To address this gap, the present study investigates the possibilities offered by some of these existing models, with some additions, for achieving GB structures consistent with the literature on DC systems.

This paper is structured such that first, the general PFC energy and dynamical equation are presented in Sec. II. Following that, the simulation geometry and the different simulation scenarios considered are presented in Sec. III. Then, three different PFC models that have been investigated are presented in Secs. IV–VI. The models' abilities for providing the appropriate GB structures and the results regarding their respective suitabilities for modeling polycrystalline DC systems are also discussed. Finally, some concluding remarks are presented in Sec. VII.

II. PFC MODEL

In this section, the general PFC free energy functional and dynamical equation used in this work are presented. Only the general form of the free energy is shown initially, with three sets of specializations, corresponding to the three DC models being investigated, detailed in Secs. IV–VI.

The total normalized PFC energy F, is generally written as a sum of the ideal gas energy F_{id} and the excess energy F_{exc} following

$$F[n(\mathbf{r})] = F_{id}[n(\mathbf{r})] + F_{exc}[n(\mathbf{r})], \quad (1)$$

which is a functional of the density field n, itself a function of the spatial coordinates $\mathbf{r}(x, y, z)$. Following [14], the ideal gas energy is expressed as

$$F_{id}[n(\mathbf{r})] = \int d\mathbf{r}\left(\frac{1}{2}n(\mathbf{r})^2 - \frac{1}{6}n(\mathbf{r})^3 + \frac{1}{12}n(\mathbf{r})^4\right). \quad (2)$$

The excess energy is adopted as an expansion up to third-order correlations, with the excess energy being a sum of the energy contributions from second-order and third-order correlations, denoted as F_2 and F_3, respectively, to provide $F_{exc} = F_2 + F_3$. In this work F_2 is defined as

$$F_2[n(\mathbf{r})] = -\frac{1}{2}\iint d\mathbf{r}d\mathbf{r}'n(\mathbf{r})n(\mathbf{r}')C_2(|\mathbf{r}' - \mathbf{r}|)$$
$$= -\frac{1}{2}\int d\mathbf{r}n(\mathbf{r})(C_2 * n)(\mathbf{r}), \quad (3)$$

where C_2 is the two-point correlation, taken to be an orientation-invariant function of the distance between the two spatial points $\mathbf{r}$ and $\mathbf{r}'$. Note that the convolution operator $*$ is introduced in Eq. (3). Finally, the third-order correlation is taken as

$$F_3[n(\mathbf{r})] = -\frac{1}{6}\iiint d\mathbf{r}d\mathbf{r}'d\mathbf{r}''n(\mathbf{r})n(\mathbf{r}')n(\mathbf{r}'')$$
$$\times C_3(\mathbf{r}' - \mathbf{r}, \mathbf{r}'' - \mathbf{r}), \quad (4)$$

where C_3 is the three-point correlation function that depends on the angle between the two vectors $\mathbf{r}' - \mathbf{r}$ and $\mathbf{r}'' - \mathbf{r}$, determined from spatial points $\mathbf{r}$, $\mathbf{r}'$, and $\mathbf{r}''$. The specific forms of C_2 and C_3 are discussed in subsequent sections.

Once the free energy has been determined, the system is set to evolve using the standard form of locally conserved dissipative dynamics through

$$\frac{\partial n}{\partial t} = M\nabla^2\frac{\delta F[n]}{\delta n}, \quad (5)$$

where the mobility constant M is set to unity in this work. A semi-implicit spectral scheme, consistent with [15], is used to solve Eq. (5). The additional contribution from third-order correlations considered in this work, not included in [15], is nonlinear and therefore is evaluated at the current time step, i.e., explicitly. A time step of 0.001 is used for all simulations. Furthermore, the grid spacing is set as close to 1/16 as possible while permitting variations to ensure correct domain sizes, as discussed in [16].

III. SIMULATION GEOMETRY AND BOUNDARY CASES

A three-dimensional (3D) periodic bicrystal geometry, with predefined symmetric tilt GBs, is used for the GB simulations, as illustrated in Fig. 1. The necessity for a periodic domain is enforced by the spectral scheme used in this work. Furthermore, the domain is initiated with two thin liquid regions, and the crystals are allowed to solidify into these regions, forming the GBs. The mean density of the liquid regions is set to the same value as for the bulk crystal. Since the GB density represents a microscopic degree of freedom (DOF) that influences the GB structure variants, or multiplicities, which are obtained [17], it is not expected that all possible boundaries can be found while keeping this value
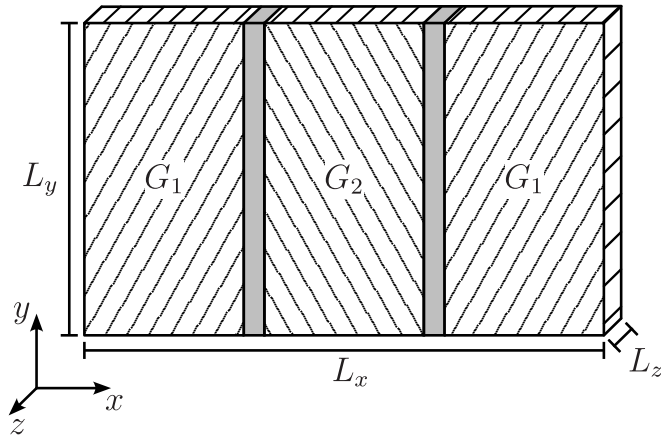
FIG. 1. Periodic 3D bicrystal geometry for two crystals G_1 and G_2 initially separated by thin liquid regions (solid gray areas) and having a common tilt axis oriented along the z axis.
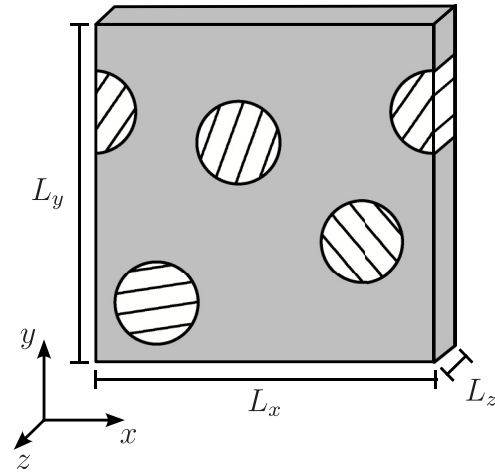

FIG. 2. Illustration of the initial geometry for the nucleation of a polycrystal. Cylindrical crystals are placed with random orientations around the $[01\bar{1}]$ axis, oriented parallel to the z axis, with the particles initially separated by a liquid region (solid gray area).

constant. However, as identification of all GB multiplicities is beyond the scope of this work, this discrepancy is not considered further. However, a full exploration of GB multiplicity by PFCs is possible, as discussed in [18].

To preserve the crystal periodicity, the domain size is chosen to be a multiple of the periodic lengths along the y and z directions for the selected crystal orientation. The periodic length is determined from the crystal direction (in Miller indices) along the coordinate axis. For example, consider the case of a (210) tilt boundary, oriented with the plane normal parallel to the x axis and with the tilt axis [001] oriented parallel to the z axis. Then $[-1, 2, 0]$ must be the crystal direction parallel to the y axis. The periodic domain dimensions are then provided by the norm of the direction described in Miller indices, i.e., $\sqrt{5}a$, a, and $\sqrt{5}a$, respectively, where a is the lattice constant, set to unity in this work for all lattices considered.

The domain length in the x direction, denoted L_x, is chosen to be large enough to accommodate any significant elastic effects caused by the presence of the two GBs. To find multiplicities of boundaries with the same macroscopic DOFs, L_x is varied in small steps and constitutes a variation of one of the microscopic DOFs. It is noted again, however, that finding all multiplicities is outside the scope of this work and only a limited part of the displacement complete lattice is searched.

A set of symmetric tilt boundaries, found in the literature [19–26], was chosen to evaluate the final GB structures obtained from the PFC simulations. This set comprises [001] tilt boundaries, including (310), (520), (210), and (320), and $[01\bar{1}]$ tilt boundaries, including (122), (111), (311), and (211).

To more clearly present and compare the modeled GB structures to those found in the literature, the maximum peak positions of the density field are interpolated, as discussed in [15], and are taken to represent the mean atomic positions. A threshold for peak identification is used, whereby only peak positions with an amplitude 30% or higher compared to the maximum peak density are included such that any small fluctuations in the density field are excluded.

A neighborhood analysis is performed around each mean atomic position to find neighboring atoms. This information

is then used to construct possible bond configurations with the requirement that each atom can form a maximum of four covalent bonds. The final bond configuration is therefore a best guess, as no explicit bonding information exists within the current PFC model. It was, however, found to be insufficient to pair atoms based on minimum distance alone, as the resulting bond networks did not match those presented in the literature. To include some weight term that encourages bond angles of $109.5°$, atom bond pairs were instead identified by finding a set of bonds that minimize the Tersoff potential energy [27], a standard potential commonly used in MD simulations of DC silicon. The Tersoff potential naturally includes terms for both bond length and angle and was found to work well in forming bonds consistent with the literature. With the use of the Tersoff potential, the minimization procedure is set up such that, atom by atom, a set of a maximum of four bond pairs was tested. If the bonding resulted in a minimization of the total Tersoff potential function, these bonds were accepted. Note that only the accepted bond pairs were included in the calculation of the atomwise Tersoff potential energy, and it was therefore not based on a cutoff distance, as is the case in MD simulations. This bond identification step was, however, solely used as a postprocessing step to visualize a possible final GB bond network, and the benefits of PFCs compared to MD persist.

Finally, to assess the phase stability of the DC crystal structure for each model, nucleation of cylindrical particles was performed in a 3D simulation domain. The model setup for such simulations is illustrated if Fig. 2.

IV. MODEL 1: SINGLE TWO-POINT CORRELATION

The first model investigated is that presented in [4], referred to as model 1 in the following. It is based on the XPFC formalism, introduced in [14], where the reciprocal of the two-point correlation function $\hat{C}_2$ is defined in Fourier space as the envelope of a sum of Gaussian peaks following

$$\hat{C}_2(\boldsymbol{k}) = \max_i \left[A_i \exp\left(-\frac{(|\boldsymbol{k}| - k_i)^2}{2\gamma_i^2} \right) \right], \qquad (6)$$
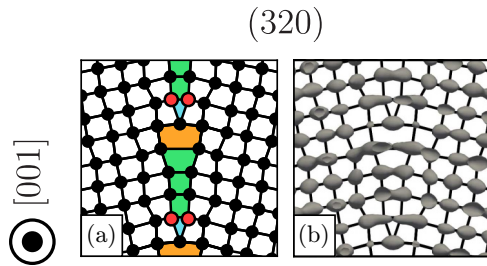
(320)

FIG. 3. Structure of the [001](320) boundary retrieved using the model presented in [4], shown both (a) as a stick-and-ball representation and (b) as contour surfaces superimposed on the bonds. The black dots in (a) represent local maxima, interpolated from the density field, and the red dots are manually added based on the contour surfaces in (b). The colored polygons in (a) are added to more clearly show the different SUs that form the boundary.

where $\boldsymbol{k}$ is the reciprocal vector, A_i is the amplitude of the ith symmetry plane, k_i is its wave number, and γ_i is the width of the Gaussian peak. Following [4], Gaussian peaks centered at $k_1 = 2\pi\sqrt{3}$ and $k_2 = 2\pi\sqrt{8}$ are used and facilitate the stabilization of the DC phase without a three-point correlation. The amplitudes are set to $A_1 = A_2 = 1$, representing a temperature of zero in [4]; $\gamma_1 = \gamma_2 = 1$, and the mean density is set to -0.05. These parameter choices position the system just right of the liquid-DC coexistence region in the phase diagram presented in [4].

While the solidification of bulk crystals worked well, out of the eight GBs considered, it was found that only the [001](320) GB, shown in Fig. 3, appeared similar to the expected GB structure. Figure 3(a) shows a stick-and-ball representation of the crystal structure, where the black dots correspond to maxima ("atoms"), interpolated in the density field, and Fig. 3(b) shows contours of the density field, with the reconstructed bond network shown in the background for clarity. The red dots represent lattice points that were added manually and are not local density peaks, but rather are part of an extended density region, as noted in the contour plot in Fig. 3(b). The colored polygons are added to show the different structural units (SUs) that make up the GB. For the other boundaries examined, broader defect structures or excessive grain growth resulting in a single grain was observed. An example of such an extended "defect" is shown in Fig. 4 and does not represent a physically feasible structure.
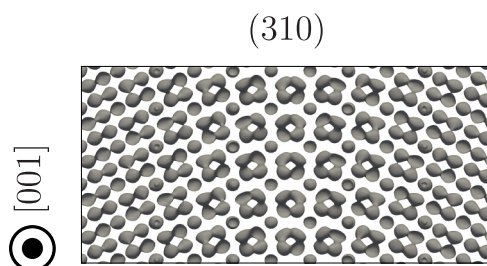
(310)

FIG. 4. Density field contour surfaces for a [001](310) boundary using model 1 based on the model presented in [4]. This type of structure is considered nonphysical.
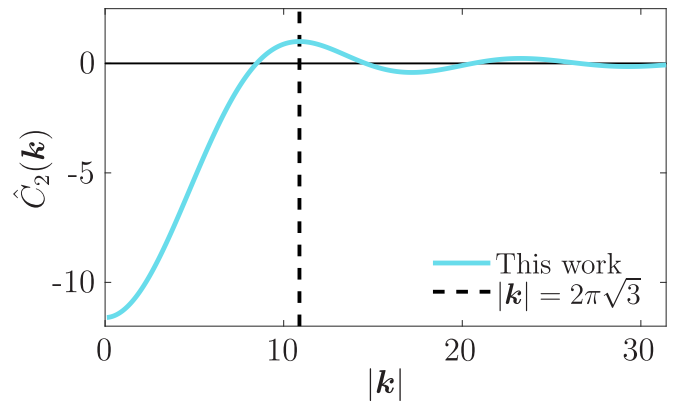

FIG. 5. Fourier transform of the repulsive correlation function [see Eq. (8)], with a maximum peak value of 1 at $|\boldsymbol{k}| = 2\pi\sqrt{3}$.

Different peak widths and numbers of peaks used in the correlation function were examined, along with different values of the mean density, but no significant improvements were found using only a two-point correlation. A main conclusion from the investigation of model 1 is therefore that using only a two-point correlation is insufficient to correctly represent the DC structure. However, using more peaks or broader peaks appeared to mitigate the wide defects shown in Fig. 4, an insight used in the third model presented in this paper (see model 3 in Sec. VI).

V. MODEL 2: USING A THREE-POINT CORRELATION

As stated in the Introduction, the model proposed in [10] shows promise due to its explicit connection to bond lengths and angles. Additionally, it has the ability to reproduce polycrystalline structures for graphene which have also been observed in experiments. Using the same ideas as presented in [10] and formulations for the three-point correlation utilized in [6], a model with an improved defect structure is obtained. This new model is referred to as model 2 in the following.

Following [10], the two-point correlation function constitutes a simple repulsive term expressed as

$$C_2(\boldsymbol{r}) = \begin{cases} -R, & \text{if } |\boldsymbol{r}| \leqslant r_0, \\ 0, & \text{otherwise,} \end{cases} \tag{7}$$

with R being the well depth and $2r_0$ being the width. The 3D Fourier transform of Eq. (7) is written as

$$\hat{C}_2(\boldsymbol{k}) = -4\pi R r_0^3 \frac{j_1(r_0|\boldsymbol{k}|)}{r_0|\boldsymbol{k}|}, \tag{8}$$

where j_1 is the first-order spherical Bessel function. Following [10], the first peak of $\hat{C}_2$ is fitted to the primary reciprocal vector of the crystal lattice, effectively controlling the length scale. Thus, setting $r_0 = 5.764/k_1$, with k_1 being the length of the main reciprocal vector, achieves this. In this case $k_1 = 2\pi\sqrt{3}$, which yields $r_0 = 0.5296$. Furthermore, R is set such that the amplitude at k_1 equals unity, which is achieved with $R = 18.66$. The final form of $\hat{C}_2$ used in this work is shown in Fig. 5.

To more accurately describe the angular dependence on neighboring lattice points, a three-point correlation is formulated in spatial coordinates. In [10], this is done to permit

2D crystals with n-fold geometry. However, this model is not directly transferable to three dimensions. Therefore, following [6], a 3D real three-point correlation function, akin to that presented in [10], can be formulated as a sum of products between directionally variant two-point correlation functions $C_2^{(lm)}$. In the general case this correlation is written as

$$C_3(\boldsymbol{r_1}, \boldsymbol{r_2}) = \sum_l^{l_{max}} \alpha_l \sum_l^{m=-l} C_2^{(lm)}(\boldsymbol{r_1}) C_2^{(lm)}(\boldsymbol{r_2}), \qquad (9)$$

where $\boldsymbol{r}_1 = \boldsymbol{r'} - \boldsymbol{r}$ and $\boldsymbol{r}_2 = \boldsymbol{r''} - \boldsymbol{r}$ and can also be identified in Eq. (4). Furthermore, α_l are weight factors given by a polynomial fit of Legendre polynomials to an angular goal function for the free energy, as described in [6], up to a total of l_{max} polynomials and with the possibility for α_l to be zero for $l < l_{max}$. Furthermore, (lm) refer to the specific real spherical harmonic function, with the integers l and m, that is included in the two-point correlation. For more details and a full derivation, the reader is referred to the Appendix. The Fourier transform of the two-point correlation functions $C_2^{(lm)}$ is written as

$$\hat{C}_2^{(lm)}(\boldsymbol{k}) = 4\pi \beta a_0^2 i^l \sqrt{\frac{4\pi}{2l+1}} Y_{lm}(\hat{\boldsymbol{k}}) j_l(k a_0) \qquad (10)$$

where β is a weight factor and a_0 can be interpreted as the bond length; in this work $a_0 = \sqrt{3}/4$. Notice that the form of Eq. (10) is similar to that given in [6], but with different radial functions. Incorporating Eq. (9) into the excess energy in Eq. (4) yields

$$F_3 = -\frac{1}{6} \sum_{l=0}^{l_{max}} \alpha_l \sum_{m=-l}^{l} \int d\boldsymbol{r} n(\boldsymbol{r}) \big(C_2^{(lm)} * n\big)^2, \qquad (11)$$

and its functional derivative is evaluated as

$$\frac{\delta F_3}{\delta n} = -\frac{1}{6} \sum_{l=0}^{l_{max}} \alpha_l \sum_{m=-l}^{l} \Big\{ \big(C_2^{(lm)} * n\big)^2$$
$$+ 2(-1)^l C_2^{(lm)} * \big[n\big(C_2^{(lm)} * n\big)\big]\Big\}, \qquad (12)$$

where the parity property of spherical harmonics has been used.

As previously mentioned, the weight factors α_l determine the angular dependence of the free energy in Eq. (11). In [6], they were set by fitting a Dirac δ distribution, which makes the calculation trivial. However, there are no formal restrictions on the form of this fitting function, and in this work a broad Gaussian is used instead to find appropriate values. This fitting yields weight factors of $\alpha_2 = -0.8$ and $\alpha_3 = 1.0$, with the remaining α_l set to zero. With these values the angular function is closer to the goal value of $109.5°$, compared to using the α_l values obtained by following the methods in [6], as shown in Fig. 6. Fewer modes are also used, which reduces the computational cost as each $C_2^{(lm)}$ that is included requires the same amount of memory as the two-point correlation C_2. Also, each included Legendre polynomial introduces $2l + 1$ correlations. Therefore, the inclusion of higher-order Legendre polynomials is more costly, both in terms of memory and because each additional mode adds some extra computations. However, as there are many ways to optimize these calculations, for example, utilizing the symmetry of the correlation functions,
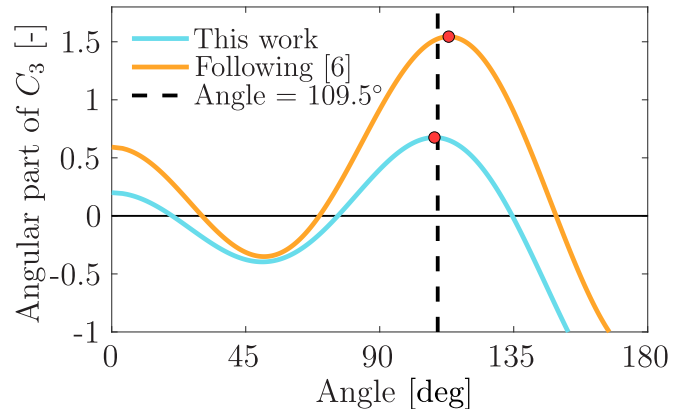

FIG. 6. The angular part of C_3 [see Eq. (9)] used in this work (blue) compared to that obtained by fitting to Dirac δ distributions (orange) with $l_{max} = 3$. Red dots indicate the maximum values of the functions.

no explicit performance comparison is demonstrated in this work.

Studying the same GBs as in the previous section by using model 2 and by setting $\beta = 0.55$, an improvement of the GB structures is observed compared to the result from using model 1, with all boundaries having sharp interfaces. However, just as with model 1, not all GB structures can be matched with those found in the literature. Only five of the nine tested boundaries matched the expected structures and are shown in Fig. 7. An example of a boundary that did not match the literature, specifically the [001](320) boundary, is shown in Fig. 8.

With the addition of sharp interfaces and good phase stability when nucleating from a domain with small dispersed particles, polycrystal simulations using model 2 are improved compared to those using model 1. An example of a polycrystal simulation is illustrated in Fig. 9, where the excess energy field is smoothed using a Gaussian kernel. This smoothing operation is applied to remove the atomic variation in the energy field, so that the local mean value can be evaluated instead. This representation is used to identify boundaries of low excess energy. Three of these boundaries correspond to symmetric tilt boundaries with typical low-energy SUs, which are extracted and also shown in Fig. 9. The other boundaries do not have symmetric tilt character, and their correspondence to real crystals has not been investigated.

If model 2 could be refined further to better capture the expected GB structures while preserving this crucial phase stability, the resulting model would hold great promise for DC
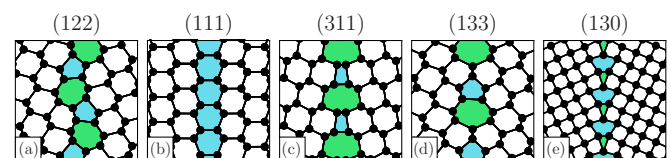

FIG. 7. Boundary structures of (a)–(d) some $[01\bar{1}]$ and (e) one [001] symmetric tilt GBs. The colored polygons are added to more clearly show the SUs that make up the boundaries.
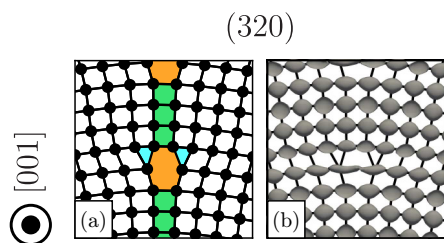
FIG. 8. GB structure of the [001](320) symmetric tilt boundary, shown both (a) as a stick-and-ball model and (b) as contour surfaces of the density field.

FIG. 10. Density contour surfaces of the [001](320) GB showing well-defined density maxima (i.e., atom positions).

simulations. Model 2 also has the potential to be extended to model other covalent systems in three dimensions.

VI. MODEL 3: A SUCCESSFUL PAIRING

The last model evaluated in this work is achieved using the two-point correlation function introduced in Sec. IV together with the three-point correlation introduced in Sec. V. This new model, hereafter referred to as model 3, performs the best in terms of GB structure formation among the models considered in this work. However, some problems regarding phase stability, compared to models 1 and 2, are identified, as will be discussed in the last part of this section.

To establish model 3, some initial modifications are made to the correlation functions of the two previous models. For the two-point correlation introduced in Sec. IV, it was found that excessively wide GBs could be remedied by using broader peaks, which results in a shorter spatial range of C_2. Setting $\gamma_i = 5$ is found to work well. Furthermore, the amplitude for the three-point correlation, introduced in Sec. V, is reduced to $\beta = 0.25$ to keep the system stable in the DC phase.

With this combination, sharp interface defects are observed, as shown in the density field contour plot in Fig. 10. It is also found that all of the simulated GBs provide the expected GB structures, including some multiplicities. These are shown for the [001] and [01$\bar{1}$] tilt boundaries in Figs. 11 and 12, respectively. Multiplicities with the same macroscopic DOFs are distinguished by subscripts $(\cdot)_i$. Of course, other boundaries were also identified for different choices of mi-

croscopic DOFs, but for the sake of clarity in the comparison between the PFC models, they are omitted in this work.

Most of the presented GBs fit those found in the literature, with two exceptions. To start with, we consider the [001] tilt boundaries in Fig. 11, where larger SUs are identified as a combination of smaller SUs, hereafter called assemblies. These assemblies are marked by capital letters and include the part of the GB between the red lines. From these constructions it is clear that the [001](520) boundaries are made up of different sets of the assemblies also identified in the [001](210), [001](310)$_1$, and [001](310)$_2$ GBs. The [001](520)$_1$ boundary represents a GB structure variant also observed in [22]. However, the formation of this second multiplicity, [001](520)$_2$, might be reasonable as [001](310)$_2$ is expected to have lower energy than that of the [001](310)$_1$ boundary according to other studies, e.g., in [21], and thus, the C assembly should yield lower GB energy than A. A thorough examination of whether this combination of GB SUs yields lower energy for the [001](520) boundary in these PFC simulations is, however, outside the scope of this work. But the GB energy can be computed, following the methodology presented in [16].

The second variation in GB structure relative to what is expected from the literature is that of the [01$\bar{1}$](122)$_1$
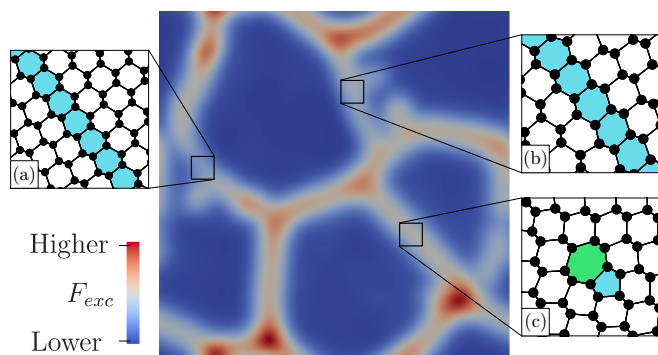

FIG. 9. A smoothed excess energy field for a polycrystal with a domain size of $50 \times 50 \times 1$. Some low-energy boundaries are identified as being made up of known low-energy SUs.
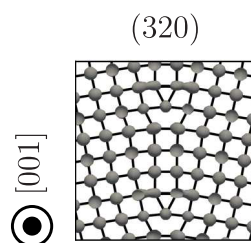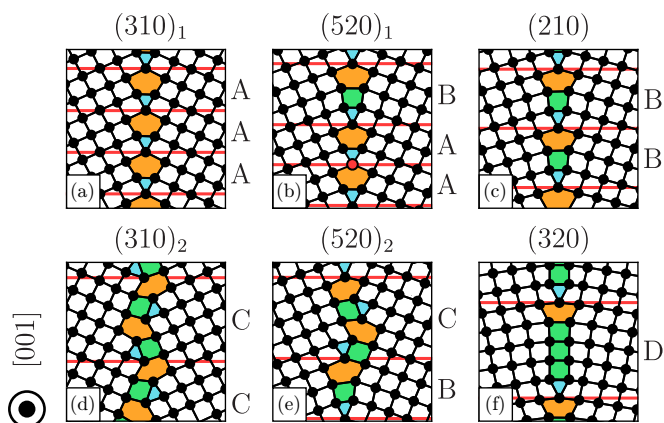

FIG. 11. GB structures of some [001] symmetric tilt GBs. Subscripts $(\cdot)_i$ refer to multiplicity ordering. The red circle was added manually in (b), as the peak had a lower amplitude than the threshold used for peak identification but still represented a local maximum. Capital letters refer to the assembly of SUs between the red lines, and the colored polygons are added to more clearly show the SUs that make up the boundaries.
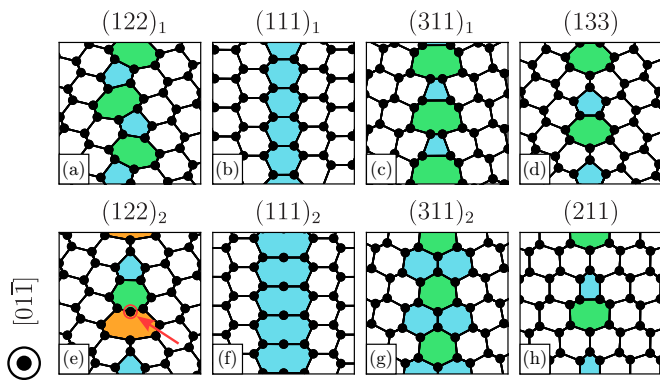
FIG. 12. GB structure of some $[01\bar{1}]$ symmetric tilt GBs. Subscripts $(\cdot)_i$ refer to multiplicity ordering. The red encircled atom in (e) indicates a difference from those found in the literature and should yield larger energy due to the unpaired atom. Furthermore, the colored polygons are added to more clearly show the SUs that make up the boundaries.

boundary, where an extra atom is present, indicated by the red circle and arrow in Fig. 12(e). From the bond optimization step using the Tersoff potential, this atom was omitted, and it instead formed a bond structure similar to that in the literature, e.g., in [25]. Thus, the bond structure was edited manually to the one presented in Fig. 12(e). Despite this, a multiplicity of $[01\bar{1}](122)$ matching that in the literature was identified. However, only the boundary with this extra atom is included to show the wide range of structures that can form. It has yet to be determined how this difference affects the PFC GB energy, as this multiplicity should result in higher energy due to the unpaired atoms.

To further compare models 2 and 3 in a more quantitative sense, the root-mean-square errors, evaluated relative to the perfect crystal state, of the bond lengths and angles are calculated for each GB included in Fig. 7. The result is shown in Fig. 13, for which the minimum and maximum atomic errors are indicated by the span of the vertical lines and the median values for all atoms considered are shown by dots. As the largest error is calculated for the GB atoms, a lower

maximum value corresponds to a better GB match to the goal bond length and angle. However, no apparent superiority can be identified for any one model in these comparisons because for some boundaries model 2 performs better and in other cases model 3 performs better.

The closing consideration is that of nucleation. In this regard model 3 does not perform fully satisfactorily because it tends to form honeycomb rod structures coexisting with the DC phase. This might not be surprising because the intersection of a honeycomb rod (forming a 2D honeycomb lattice) has 120° bond angles similar to those of DC. In simulations of a 3D domain initiated as a liquid with small dispersed particles, the domain tends to form three distinct phases: DC regions with the prescribed mean density, honeycomb rods in regions with larger mean density, and liquid in (depleted) regions of lower mean density. However, if a polycrystal is initiated as fully occupied by grains with DC structure, it tends to be stable in most cases, without any decomposition of the mean density.

To find more appropriate model parameters for which only the DC phase exists, a phase diagram would be beneficial. It would then become apparent whether there are parameter values for which only DC exists. However, due to the complexity of the model, it would not be adequate to just use the low mode approximation, as done in [28]. Instead, a numerical model akin to that used in [29] would have to be used. This approach would, however, introduce additional complexities such as small variations of the lattice spacing for different mean densities and between the DC and honeycomb rod phases. Such model development is outside the scope of the current study but should be considered in further development of model 3.

Last, the formation of the honeycomb rod phase and the instability of the DC phase can likely be attributed to the use of broad Gaussian peaks, as similar structures emerged when the single two-point correlation function with equally broad peaks was used. This is consistent with what was found in, e.g., [30], where it was concluded that broad correlation kernels led to higher defect stability at the expense of crystal stability, similar to what is found here. The emergence of the honeycomb rod phase might be mitigated by employing the vacancy PFC method introduced in [31], where a local nonlinear cutoff
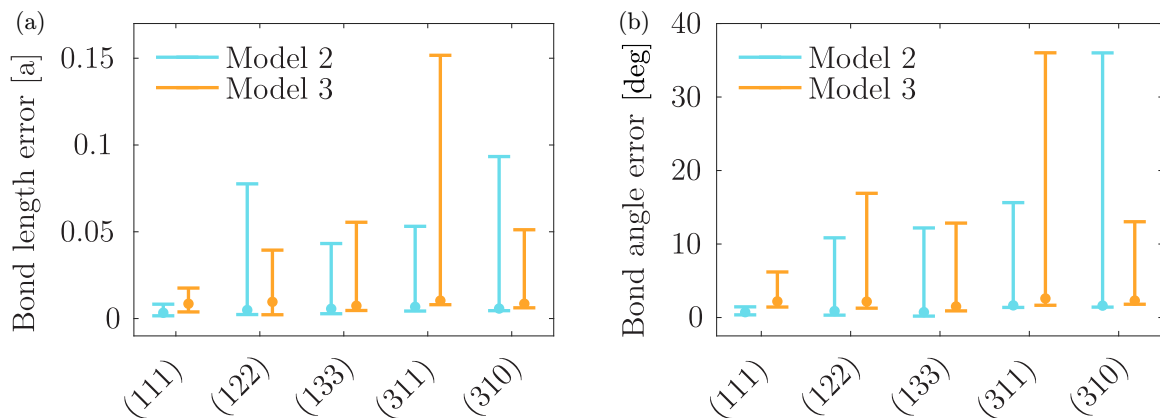

FIG. 13. Root-mean-square errors, evaluated relative to the perfect crystal state, for (a) the bond lengths and (b) angles for atoms in a GB region of matching multiplicities retrieved using both models 2 and 3. The range of values calculated for all atoms in a region containing a GB is indicated by a vertical line, and a dot indicates the median of all values.

was included, which strongly discourage one-mode solutions. This addition has yet to be tested and is left for future work.

VII. CONCLUSIONS AND FINAL REMARKS

In this work, three different PFC models for DC systems were investigated. These tests concluded that simulation of DC systems using the PFC framework is more challenging than more commonly studied metallic systems, such as fcc and bcc systems, which fit established results regarding, e.g., GB structure and energy [16]. Despite this, two promising avenues were identified in models 2 and 3 using a three-point correlation function defined in spatial coordinates, with expected GB structures successfully stabilized. However, model 2 is able to stabilize only some of the expected GB structures considered in this work. For these GBs the structures are comparable to those found with model 3. These results might be improved by introducing an attractive part similar to that used in the quasiparticle approach [12]. This added degree of freedom might allow for better control of the low-energy defects.

Finally, in the considered models there seems to be a compromise needed between defect and phase stability, similar to that shown in [30]. This was especially noted for model 3. However, if the energy of the honeycomb rod phase can be reduced such that this phase does not form, model 3 is likely to work well for DC simulations. It is noted that the inclusion of a stabilization term like that in [9] or a local nonlinear cutoff term similar to that in [31] can be used to stifle the growth of a honeycomb rod phase.

ACKNOWLEDGMENTS

APPENDIX: A 3D REAL THREE-POINT CORRELATION

The derivation of the three-point correlation function used in this work is presented here. It can be seen as a 3D extension of the correlation presented in [10] or a variation of that derived in [6]. The three-point correlation function $C_3(\boldsymbol{r}_i, \boldsymbol{r}_j, \boldsymbol{r}_k) = C_3(\boldsymbol{r}_j - \boldsymbol{r}_i, \boldsymbol{r}_k - \boldsymbol{r}_i) = C_3(\boldsymbol{r}_1, \boldsymbol{r}_2)$ is devised such that it minimizes the energy for points located a certain distance from a center point, $|\boldsymbol{r}_1| = |\boldsymbol{r}_2| = a_0$, forming a specific angle $\theta_0 = \arccos[\boldsymbol{r}_1 \cdot \boldsymbol{r}_2/(|\boldsymbol{r}_1||\boldsymbol{r}_2|)]$. For this purpose it is defined in spatial coordinates similar to what is done in [10], while a definition in reciprocal space is used in [6].

Following [6], the computations will be easier if a form of C_3 can be found such that

$$C_3(\boldsymbol{r}_1, \boldsymbol{r}_2) = \sum_i C_3^{(i)}(\boldsymbol{r}_1) C_3^{(i)}(\boldsymbol{r}_2). \tag{A1}$$

To achieve this the following ansatz is made:

$$C_3(\boldsymbol{r}_1, \boldsymbol{r}_2) = \beta^2 R(|\boldsymbol{r}_1|) R(|\boldsymbol{r}_2|) \sum_{l=0}^{l_{max}} \alpha_l P_l(\hat{\boldsymbol{r}}_1 \cdot \hat{\boldsymbol{r}}_2), \tag{A2}$$

where β is a constant, R is some radial function, α_l are weights for the Legendre polynomials P_l, and $\hat{\boldsymbol{r}}_i = \boldsymbol{r}_i/|\boldsymbol{r}_i|$. As the Legendre polynomials form an orthogonal basis, any continuous angular function can be represented. Using additional terms will, however, increase the computational effort. It can be noted that the difference from [6] is that Eq. (A2) is expressed in spatial coordinates, instead of in reciprocal space. This was done to get a more direct representation of the bonding characteristics for atoms in the DC structure, like in [10].

The Legendre polynomials can be written as a sum of real spherical harmonics, such that Eq. (A2) takes the form

$$C_3(\boldsymbol{r}_1, \boldsymbol{r}_2) = \beta^2 R(|\boldsymbol{r}_1|) R(|\boldsymbol{r}_2|) \sum_{l=0}^{l_{max}} \alpha_l$$

$$\times \sum_{m=-l}^{l} \frac{4\pi}{2l+1} Y_{lm}(\hat{\boldsymbol{r}}_1) Y_{lm}(\hat{\boldsymbol{r}}_2), \tag{A3}$$

from which the two-point correlation $C_2^{(lm)}$ can be identified as

$$C_2^{(lm)}(\boldsymbol{r}) \equiv \sqrt{\frac{4\pi}{2l+1}} \beta R(|\boldsymbol{r}|) Y_{lm}(\hat{\boldsymbol{r}}) \tag{A4}$$

such that

$$C_3(\boldsymbol{r}_1, \boldsymbol{r}_2) = \sum_l^{l_{max}} \alpha_l \sum_l^{m=-l} C_2^{(lm)}(\boldsymbol{r}_1) C_2^{(lm)}(\boldsymbol{r}_2). \tag{A5}$$

Equation (A5) is the form expressed in Eq. (A1) and is identical to that given in [6], except that the $(-i)^l$ term was omitted because it is not needed to keep $C_2^{(lm)}$ real. When using a spectral method to solve the PFC equation, the Fourier transform of Eq. (A4) is desirable. This can be found as

$$\hat{C}_2^{(lm)}(\boldsymbol{k}) = \sqrt{\frac{4\pi}{2l+1}} \beta \int R(r) Y_{lm}(\hat{\boldsymbol{r}}) e^{i\boldsymbol{r}\cdot\boldsymbol{k}} d\boldsymbol{r}, \tag{A6}$$

where $r = |\boldsymbol{r}|$. Using a plane wave expansion, this can be written in the form

$$\hat{C}_2^{(lm)}(\boldsymbol{k}) = \sqrt{\frac{4\pi}{2l+1}} \beta \int R(r) Y_{lm}(\hat{\boldsymbol{r}}) 4\pi$$

$$\times \sum_{l'=0}^{\infty} \sum_{m'=-l'}^{l'} i^{l'} j_{l'}(kr) Y_{l'm'}(\hat{\boldsymbol{r}}) Y_{l'm'}(\hat{\boldsymbol{k}}) d\boldsymbol{r} \tag{A7}$$

Reformulating Eq. (A7) in spherical coordinates and moving the sum outside the integral result in

$$\hat{C}_2^{(lm)}(\boldsymbol{k}) = \sqrt{\frac{4\pi}{2l+1}} \beta 4\pi \sum_{l'=0}^{\infty} \sum_{m'=-l'}^{l'} i^{l'} Y_{l'm'}(\hat{\boldsymbol{k}}) \int j_{l'}(kr) R(r) r^2 dr$$

$$\times \int Y_{lm}(\theta, \phi) Y_{l'm'}(\theta, \phi) \sin\theta d\theta d\phi. \tag{A8}$$

It is apparent that due to the orthogonality of the normalized spherical harmonics, the last integral in Eq. (A8) is

evaluated to $\delta_{l'l}\delta_{m'm}$, with δ being the Kronecker delta. Thus, Eq. (A8) is reduced to

$$\hat{C}_2^{(lm)}(\boldsymbol{k}) = \sqrt{\frac{4\pi}{2l+1}}\beta 4\pi i^l Y_{lm}(\hat{\boldsymbol{k}})\int j_l(kr)R(r)r^2 dr. \quad (A9)$$

The only thing left is to determine a suitable form for the radial function R. Following the choice made in [10], the radial function is chosen to be $R(r) = \delta(r - a_0)$, where a_0 can

be interpreted as the bond length. The Fourier transform of $C_2^{(lm)}(\boldsymbol{r})$ then becomes

$$\hat{C}_2^{(lm)}(\boldsymbol{k}) = 4\pi\beta a_0^2 i^l \sqrt{\frac{4\pi}{2l+1}}Y_{lm}(\hat{\boldsymbol{k}})j_l(ka_0). \quad (A10)$$

All components of the three-point correlation function used in the present work are thereby available.

[1] P. Škarvada, P. Tománek, P. Koktavý, R. Macků, J. Šicner, M. Vondra, D. Dallaeva, S. Smith, and L. Grmela, A variety of microstructural defects in crystalline silicon solar cells, Appl. Surf. Sci. **312**, 50 (2014).

[2] D. Kohler, A. Zuschlag, and G. Hahn, On the origin and formation of large defect clusters in multicrystalline silicon solar cells, Sol. Energy Mater. Sol. Cells **120**, 275 (2014).

[3] R. D. Kamachali, A model for grain boundary thermodynamics, RSC Adv. **10**, 26728 (2020).

[4] V. W. L. Chan, N. Pisutha-Arnond, and K. Thornton, Phase-field crystal model for a diamond-cubic structure, Phys. Rev. E **91**, 053305 (2015).

[5] S. V. Rodriguez, M. Frick, N. Quitoriano, N. Ofori-Opoku, N. Provatas, and K. H. Bevan, Capturing dislocation half-loop formation and dynamics in epitaxial growth atomistically at diffusive time scales, Materialia **20**, 101253 (2021).

[6] E. Alster, D. Montiel, K. Thornton, and P. W. Voorhees, Simulating complex crystal structures using the phase-field crystal model, Phys. Rev. Mater. **1**, 060801(R) (2017).

[7] Z. -L. Wang, Z. Liu, and Z. Huang, Angle-adjustable density field formulation for the modeling of crystalline microstructure, Phys. Rev. B **97**, 180102(R) (2018).

[8] Z. -L. Wang, Z. Liu, W. Duan, and Z. Huang, Control of phase ordering and elastic properties in phase field crystals through three-point direct correlation, Phys. Rev. E **105**, 044802 (2022).

[9] M. De Donno, L. Benoit-Maréchal, and M. Salvalaglio, Amplitude expansion of the phase-field crystal model for complex crystal structures, Phys. Rev. Mater. **7**, 033804 (2023).

[10] M. Seymour and N. Provatas, Structural phase field crystal approach for modeling graphene and other two-dimensional structures, Phys. Rev. B **93**, 035447 (2016).

[11] M. C. Rechtsman, F. H. Stillinger, and S. Torquato, Synthetic diamond and wurtzite structures self-assemble with isotropic pair interactions, Phys. Rev. E **75**, 031403 (2007).

[12] M. Lavrskyi, H. Zapolsky, and A. G. Khachaturyan, Quasiparticle approach to diffusional atomic scale self-assembly of complex structures: from disorder to complex crystals and double-helix polymers, npj Comput. Mater. **2**, 15013 (2016).

[13] F. H. Stillinger and T. A. Weber, Computer simulation of local order in condensed phases of silicon, Phys. Rev. B **31**, 5262 (1985).

[14] M. Greenwood, N. Provatas, and J. Rottler, Free energy functionals for efficient phase field crystal modeling of structural phase transformations, Phys. Rev. Lett. **105**, 045702 (2010).

[15] K. H. Blixt and H. Hallberg, Grain boundary and particle interaction: Enveloping and pass-through mechanisms studied by 3D phase field crystal simulations, Mater. Des. **220**, 110845 (2022).

[16] K. H. Blixt and H. Hallberg, Evaluation of grain boundary energy, structure and stiffness from phase field crystal simulations, Modell. Simul. Mater. Sci. Eng. **30**, 014002 (2022).

[17] J. Hickman and Y. Mishin, Extra variable in grain boundary description, Phys. Rev. Mater. **1**, 010601(R) (2017).

[18] H. Hallberg and K. H. Blixt, Multiplicity of grain boundary structures and related energy variations, Mater. Today Commun. **38**, 107724 (2024).

[19] M. Kohyama, Structures and energies of symmetrical ⟨001⟩ tilt grain boundaries in silicon, Phys. Status Solidi B **141**, 71 (1987).

[20] T. Yokoi, Y. Noda, A. Nakamura, and K. Matsunaga, Neural-network interatomic potential for grain boundary structures and their energetics in silicon, Phys. Rev. Mater. **4**, 014605 (2020).

[21] M. Guziewski, A. D. Banadaki, S. Patala, and S. P. Coleman, Application of Monte Carlo techniques to grain boundary structure optimization in silicon and silicon-carbide, Comput. Mater. Sci. **182**, 109771 (2020).

[22] C. Kohler, Atomistic modelling and of structures and of tilt and grain and boundaries and antiphase and boundaries in ß-silicon carbide, Phys. Status Solidi B **234**, 522 (2002).

[23] M. G. Tsoutsouva, P. E. Vullum, K. Adamczyk, M. Di Sabatino, and G. Stokkan, Interfacial atomic structure and electrical activity of nano-facetted CSL grain boundaries in high-performance multi-crystalline silicon, J. Appl. Phys. **127**, 125109 (2020).

[24] M. Kohyama, R. Yamamoto, and M. Doyama, Structure and energies of symmetrical ⟨011⟩ tilt grain boundaries in silicon, Phys. Status Solidi B **137**, 11 (1986).

[25] L. Wang, W. Yu, and S. Shen, Revisiting the structures and energies of silicon ⟨110⟩ symmetric tilt grain boundaries, J. Mater. Res. **34**, 1021 (2019).

[26] L. Sun, M. A. L. Marques, and S. Botti, Direct insight into the structure-property relation of interfaces from constrained crystal structure prediction, Nat. Commun. **12**, 811 (2021).

[27] J. Tersoff, New empirical approach for the structure and energy of covalent systems, Phys. Rev. B **37**, 6991 (1988).

[28] K. R. Elder, M. Katakowski, M. Haataja, and M. Grant, Modeling elasticity in crystal growth, Phys. Rev. Lett. **88**, 245701 (2002).

[29] A. Jaatinen and T. Ala-Nissila, Extended phase diagram of the three-dimensional phase field crystal model, J. Phys.: Condens. Matter **22**, 205402 (2010).

[30] J. Berry, N. Provatas, J. Rottler, and C. W. Sinclair, Defect stability in phase-field crystal models: Stacking faults and partial dislocations, Phys. Rev. B **86**, 224112 (2012).

[31] P. Y. Chan, N. Goldenfeld, and J. Dantzig, Molecular dynamics on diffusive time scales from the phase-field-crystal equation, Phys. Rev. E **79**, 035701(R) (2009).